Journal of Natural Gas Science and Engineering 105 (2022) 104719

Contents lists available at ScienceDirect

Journal of Natural Gas Science and Engineering

journal homepage: www.elsevier.com/locate/jngse

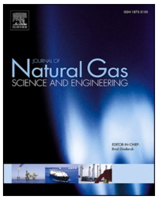

Statistical and neural network analysis of the relationship between the stochastic nature of pore connectivity and flow properties of heterogeneous rocks

Olubukola Ishola [a], Aaron Alexander [b], Javier Vilcáez [a,*]

[a] *Boone Pickens School of Geology, Oklahoma State University, Stillwater, OK, 74078, USA*
[b] *Mechanical Engineering Technology, Oklahoma State University, Stillwater, OK, 74078, USA*

ARTICLE INFO

Keywords:
Carbonate rocks
Pore-scale modeling
Permeability and hydraulic tortuosity
Heterogeneity
Pore connectivity
Machine learning

ABSTRACT

We used a stochastic 3D pore-scale simulation approach to statistically elucidate the effect of stochastic pore connectivity on permeability and hydraulic tortuosity of highly heterogeneous porous media such as carbonate rocks. The novel nature of our workflow lies in the generation of multiple 3D pore microstructures of the same effective porosity, pore size distribution, number of pores, but different stochastic pore connectivity where the only pore microstructural feature changing is pore connectivity. This workflow allows the explicit study of the role pore connectivity plays in permeability and hydraulic tortuosity without the interference of other pore microstructural factors or noise. Permeability and hydraulic tortuosity of the 3D pore microstructures of the aforementioned characteristics was obtained from direct pore-scale simulations using STAR CCM+. Our approach suppresses the necessity of conducting hundreds of experimental measurements and allows the training of neural network models to predict permeability and hydraulic tortuosity. We show that an approximate twofold increase in heterogeneity (pore size standard deviation), results in a two orders of magnitude reduction in permeability, and that an increase in heterogeneity results in a systematic shift of permeability from normal distribution to lognormal distribution. While the stochastic connectivity of pores has a significant impact on permeability, it has only minimal effect on hydraulic tortuosity. Furthermore, the predictability of permeability from hydraulic tortuosity decreases with an increasing heterogeneity. The high coefficient of determination obtained in permeability prediction with a feedforward neural network (NN) model trained with of PTSD data along with pore surface area parameters indicates that NN algorithms can capture the effect of stochastic pore connectivity on permeability. Since PTSD data and surface parameters can be obtained from mercury injection capillary pressure (MICP) measurements, our findings have large implication toward the prediction of permeability and hydraulic tortuosity in highly heterogeneous porous media.

1. Introduction

Predictions of subsurface flow processes requires knowing the flow and transport properties of subsurface porous media, among which permeability and hydraulic tortuosity are the main flow and transport properties dictating flow of fluids and transport of solutes. Permeability is the ease of fluid flow through porous media (Friedman, 1976; Zhang, 2013) and hydraulic tortuosity is the ratio of actual flow path length to the straight-line distance between ends of the flow path (Carman, 1937; Clennell, 1997; Kozeny, 1927). Permeability of porous media is traditionally computed from deterministic model equations that relate permeability to other properties such as porosity, sphericity of grains, hydraulic tortuosity, and surface area (Carman, 1937; Kozeny, 1927). While permeability values obtained from deterministic equations are relatively effective to predict the flow of fluids in homogeneous porous media such as siliciclastic rocks and soil materials, they do not always suit flow prediction in highly heterogeneous porous media such as carbonate rocks (He et al., 2014). The use of porosity as the key parameter in estimating permeability of carbonate rocks is known to be very erratic. It has been shown that a single porosity value can have a five-order of magnitude range in permeability (Westphal et al., 2005a). This is due to the complex pore microstructure of carbonate sedimentary rocks. Fundamentally, flow and transport properties of porous media are a function of pore size distribution and random pore connectivity that

---

[*] Corresponding author.
E-mail address: vilcaez@okstate.edu (J. Vilcáez).

https://doi.org/10.1016/j.jngse.2022.104719
Received 25 April 2022; Received in revised form 12 June 2022; Accepted 13 July 2022

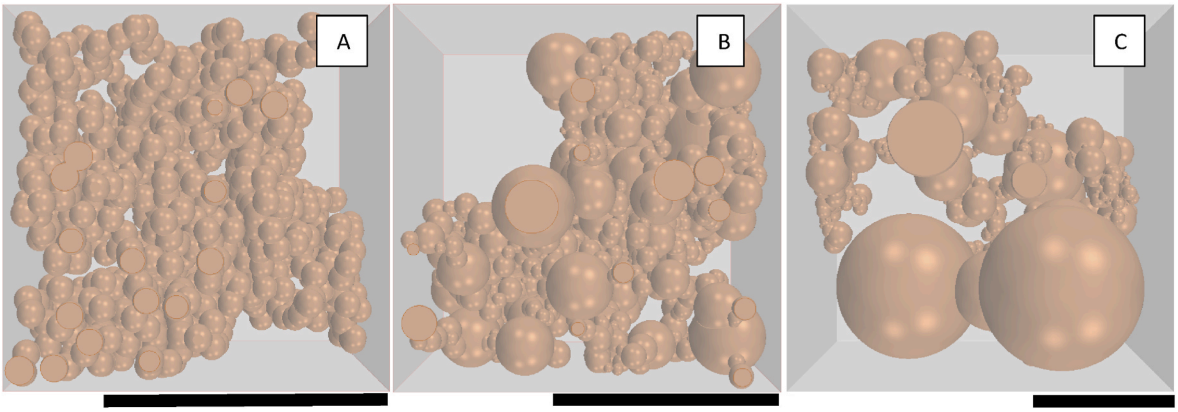

Fig. 1. Representative 3D pore-microstructures of stochastic pore connectivity. A) group I: 0 μm pore size standard deviation, B) group II: 5 μm pore size standard deviation, and C) group III: 11 μm pore size standard deviation. The mean pore size is 10 μm in all three groups. The brown spherical balls are the pores while the background is the solid matrix. The black bar represents 100 μm in the respective images.

can result in complex heterogeneous pore microstructures (Algive et al., 2012; Chen et al., 2015; Cheng et al., 2019). Pore connectivity describes the degree of connection between pores in a rock. The magnitude of pore connectivity is the sum of the effects of pore-throat sizes (Dutton and Loucks, 2010) and the average number of pores connected to a single pore in a rock (Dutton and Loucks, 2010; Bernabé et al., 2010). Capturing the complexity of pore connectivity in carbonate rocks requires stochastic models (Whitten, 1977). This has been shown to better represent flow behavior in complex heterogeneous systems compared to deterministic approaches (Apostolopoulou et al., 2019).

To consider the effect of pore size distribution, permeability can be estimated from Nuclear Magnetic Resonance (NMR) data using the Timur-Coates (TC) equation (Timur, 1968) and the Schlumberger-Doll-Research (SDR) equation (Kenyon, 1992). The use of pore size distributions has been shown to yield more accurate rock permeability values compared to the sole use of porosity (Westphal et al., 2005b). That said, its application in carbonate sedimentary rocks is still problematic due to heterogeneity (Choquette and Pray, 1970) and pore connectivity (Westphal et al., 2005b). This is because the TC and SDR equations assume that pores are evenly distributed and evenly connected which is not true (Westphal et al., 2005b). In fact, these model equations are known to over-estimate permeability due to the use of total porosity instead of effective porosity as the porosity parameter (Westphal et al., 2005b).

Mercury injection capillary pressure (MICP) is another tool employed to estimate permeability of rocks of complex pore microstructures through empirical model equations (Dastidar et al., 2007; Kamath, 1992; Kolodzie, 1980; Pittman, 1992; Purcell, 1949; Swanson, 1981; Walls and Amaefule, 1985). MICP provides pore-throat size distributions within a rock. The use of MICP data in predicting permeability usually relies on a percentage of mercury saturation in a rock sample (Kamath, 1992; Kolodzie, 1980; Pittman, 1992; Purcell, 1949; Swanson, 1981; Walls and Amaefule, 1985) or a weighted average of pore-throat sizes obtained from MICP (Dastidar et al., 2007) and do not fully account for pore connectivity. Other methods employed in obtaining pore size distribution of rocks includes the use of scanning electron microscope (SEM), focused ion beam-scanning electron microscope (FIB-SEM), micro-CT scanners, and gas adsorption techniques (Anovitz and Cole, 2015; Blunt et al., 2013; Xiong et al., 2016).

Like permeability, hydraulic tortuosity is usually estimated from deterministic model equations that employs porosity as the key parameter (Kimura, 2018; Lala, 2020). Such estimates of hydraulic tortuosity might also mislead in reactive and/or solute transport simulations given that size of individual pores and their connectivity might play a significant role in the path through which solutes are transported in complex pore microstructures.

At present, a predictive understanding of the relationship between complex pore microstructure and flow properties of carbonate sedimentary rocks is not fully developed (Bijeljic et al., 2013; Zhang and Cai, 2021), leading to the reliance on empirically derived permeability and hydraulic tortuosity properties obtained by analogy or statistical analysis of past data (England et al., 1994). This is associated with enhanced oil recovery, geological carbon storage (Shabani et al., 2020; Shabani and Vilcáez, 2017, 2018, 2019; Vilcáez, 2015), and petroleum produced water disposal (Ebrahimi and Vilcáez, 2018a, 2018b, 2019; Vilcáez, 2020), for instance.

To improve this understanding, this study employs a stochastic pore-scale simulation approach. The approach consists of constructing hundreds of 3D pore microstructures of the same effective porosity, pore size distribution, number of pores, but different stochastic pore connectivity, just like it happens in rock samples. Permeability and hydraulic tortuosity of the constructed 3D pore microstructures of the aforementioned characteristics are obtained from direct pore-scale simulations. The use of direct pore-scale simulations to obtain permeability and hydraulic tortuosity is a standard practice in pore-scale modeling (Soete et al., 2017; Vilcáez et al., 2017). Our hypothesis is that enough pore microstructures where the only pore microstructural feature changing is pore connectivity allows improved investigation into the role of pore connectivity in fluid flow without the interference of other factors. Furthermore, it will help assess the predictability of pore-scale permeability and hydraulic tortuosity without explicit inclusion of pore connectivity in feedforward neural network (NN) models.

Feedforward NN is a type of artificial neural network architecture where neurons are grouped by layers and connections which only move in the direction of the output (Mendes et al., 2002; Erofeev et al., 2019; Al Khalifah et al., 2020). NN is chosen as the machine learning algorithm for this study because of its ability to deduce the best set of weights that map a set of input features to the desired target. This ability is useful in this study because pore connectivity is random, and it is the only pore microstructural parameter varying. Hence, the random nature of pore connectivity is captured by NN if accuracy of prediction on test dataset is high. Other popular NN approaches in geosciences includes convolutional neural network (CNN) which is often used for making predictions from image data (Graczyk and Matyka, 2020; Tembely et al., 2021) and recurrent neural networks (RNN) which was developed for sequential or time series data (Jiang et al., 2021; Song et al., 2020). More recently, Bayesian neural networks (BNN) are being used to take uncertainty into account and overcome overfitting which is one of the principal challenges of neural networks (Feng et al., 2021a, 2021b).

The novel nature of our workflow lies in the generation of multiple pore microstructures where the only pore microstructural feature changing is pore connectivity. This workflow allows elucidation of the

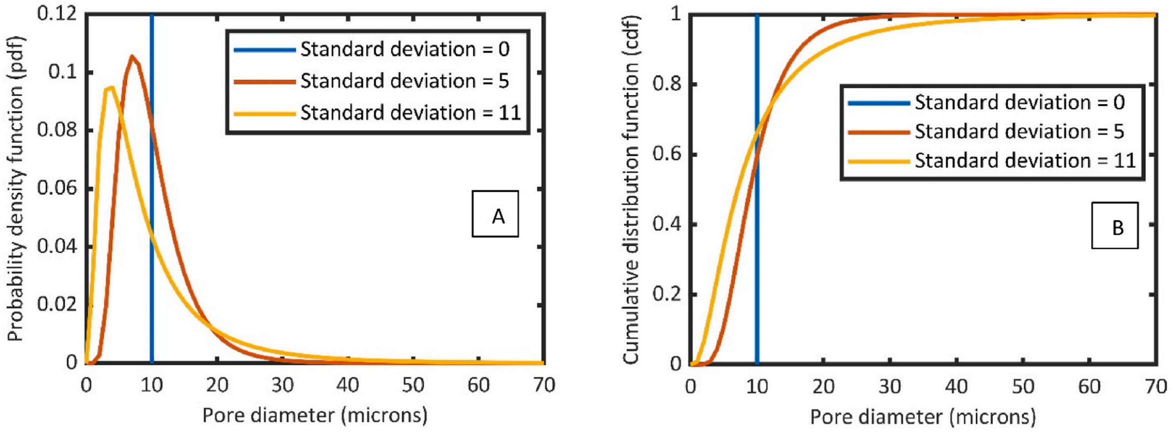

Fig. 2. Lognormal pore size distribution (PSD) curves employed to generate the 3D pore microstructures of stochastic pore connectivity. A) shows the probability density function (pdf) while B) is the corresponding cumulative distribution function (cdf). A pore size standard deviation of 0, 5, and 11 μm represents group I, II, and III respectively. The mean pores size is 10 μm in all three groups.

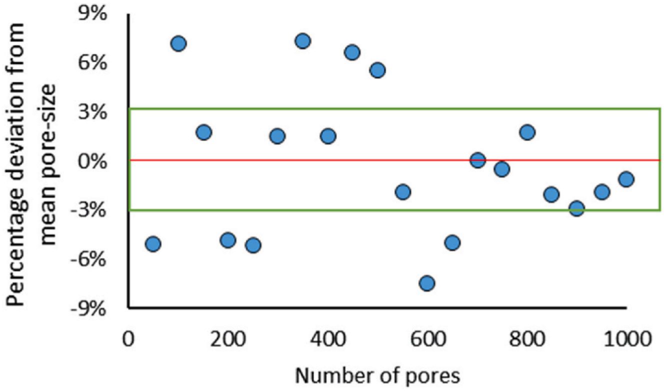

Fig. 3. Mean pore size REV analysis showing a minimum of 700 pores can be deemed representative because the percentage deviation from mean (red line) is within 3% (green box) when the number of pores is increased further.

2. Methods

2.1. Stochastic construction of 3D pore microstructures

To elucidate the effect of random pore connectivity on permeability and hydraulic tortuosity of highly heterogeneous porous media, three groups of 3D pore microstructures were generated. The 3D pore microstructures in each group had the same pore size distribution and effective porosity but different stochastic connectivity between the pores (Fig. 1).

The input data used to generate each group of the 3D pore microstructures are pore geometry, effective porosity, and pore size distribution (PSD). Spheres were used as the pore geometry in this study because the focus is on pore connectivity, thus, we needed to constrain role pore connectivity on permeability and hydraulic tortuosity without the interference of other pore microstructural factors, noise, and/or assumptions. Hence, we can determine the degree of influence of pore connectivity on pore microstructures with respect to set levels of heterogeneity and evaluate if NN models capture the stochastic nature of pore connectivity.

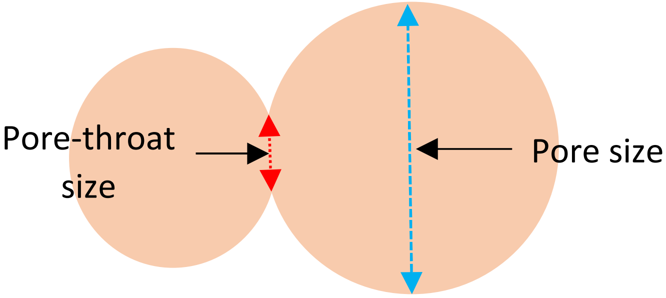

Fig. 5. A schematic comparing pore-throat (red line) and pore size (blue line).

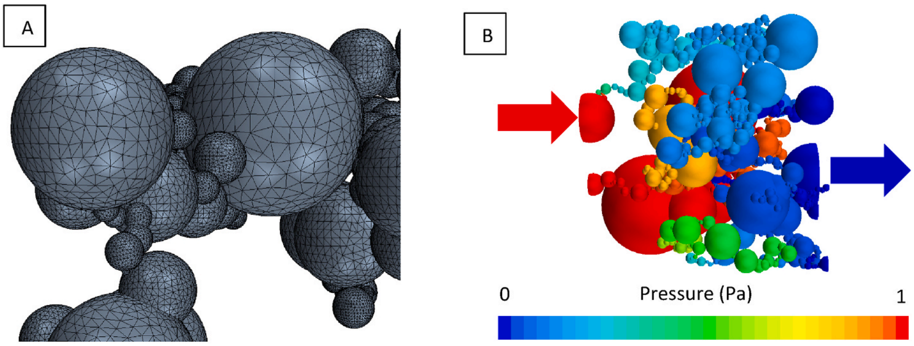

Fig. 4. Pore-scale simulations. A) A polyhedral mesh type was applied to adequately capture the complex nature of a 3D-pore-microstructure. The average pore size is 10 μm while the minimum cell size of the mesh is 0.75 μm. B) Representative pressure distribution across a 3D pore microstructure at steady state conditions. The inlet is on the left (red arrows) and the outlet is on the right (blue arrows).

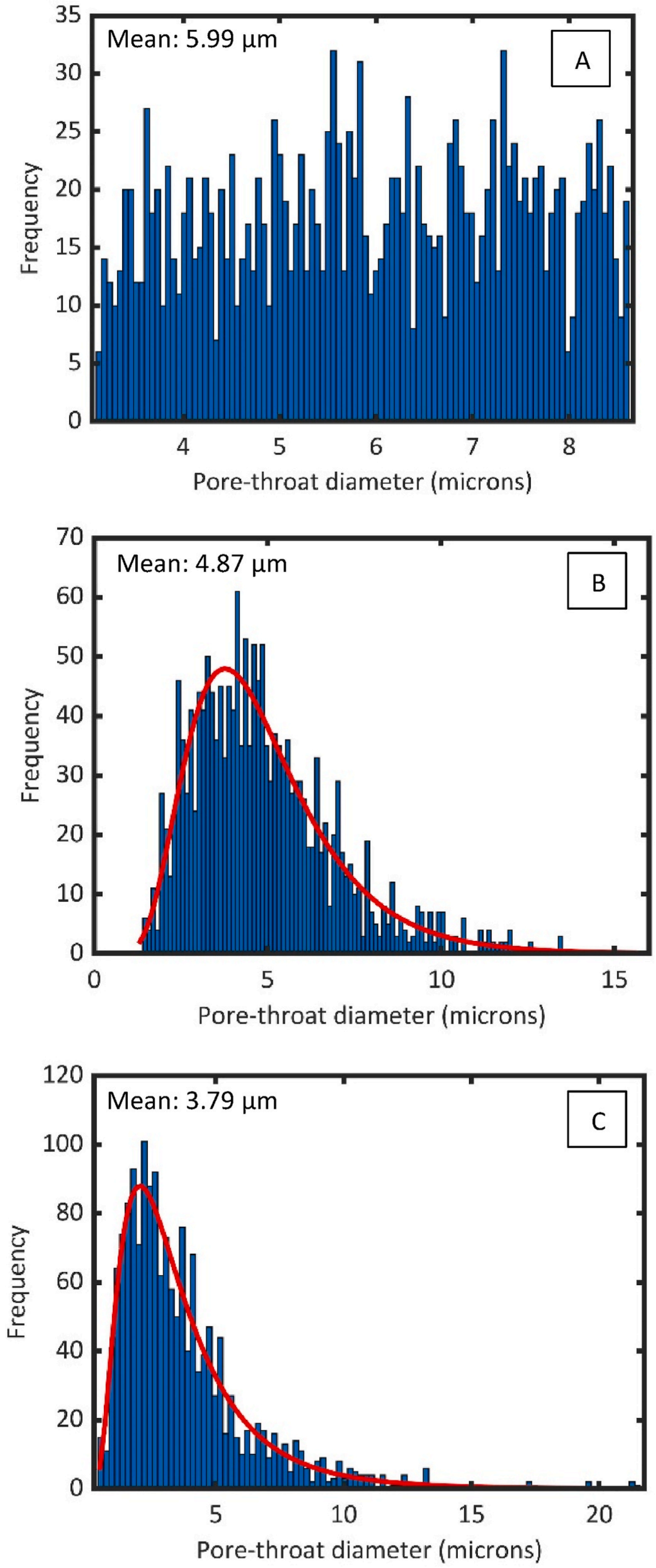

Fig. 6. Histogram of pore-throat size distribution of a single 3D pore microstructure for A) group I, B) group II, and C) group III.

pore geometry. It is noteworthy that the use of spherical pores is routine in pore network modelling (Huang et al., 2020; Zheng et al., 2022; Baychev et al., 2019; Yang et al., 2018). The effective porosity of all the generated 3D pore microstructures is consistent with an average of 19% and a coefficient of variation of 1%. Coefficient of variation (CV) reflects the degree of variation in data from the mean. CV is mathematically expressed as:

$$CV = \frac{Standard\ deviation}{m} * 100 \tag{1}$$

$$Standard\ deviation = \sqrt{\frac{1}{n}\sum_{i=1}^{n}(D_i - m)^2} \tag{2}$$

where n is the number of pores, D_i is the diameter of pore i, and m is the mean diameter of the pores.

Lognormal distribution curves were used to represent PSD because of their frequent use to describe PSD of rocks (Ding et al., 2015; Huang et al., 2019; Li et al., 2020; Munawar et al., 2021; Naraghi and Javadpour, 2015; Niu and Zhang, 2018). For this study, the mean pore size of all generated 3D pore-microstructures is 10 μm with a pore size standard deviation of 0, 5, and 11 μm for groups I, II, and III, respectively (Fig. 2).

While the average pore size in rocks can vary widely, a dominant pore size of about 10 μm has been reported for different diagenetic stages of carbonate rocks (van der Land et al., 2013). The increase in standard deviation in each group is to mimic different levels of heterogeneity in real rock samples. By implication, group I with a standard deviation of 0 is comprised of pores of the same sizes but stochastic pore connectivity (Fig. 1.A) and a higher pore size standard deviation corresponds to an increased degree of heterogeneity in PSD (Fig. 1.B and 1. C). Groups I, II, and III comprises of 991, 990, and 805 3D pore-microstructures respectively. The average number of pores in each 3D pore microstructures was 973 with a CV of 3% across all the generated 3D pore microstructures. The number of pores in all three groups of 3D pore microstructures are practically the same to suppress the effect of number of pore-throats on permeability and hydraulic tortuosity.

The generation of 3D pore microstructures of stochastic pore connectivity was done using statistical tools on MATLAB together with the CAD capabilities of STAR CCM+® (a computational fluid dynamics software by Siemens). The procedure consisted of the generation of random sizes of pores based on a given mean pore size and standard deviation of the PSD curve. The coordinates of pores and thus the stochastic connectivity between pores in the 3D pore microstructure was decided using a uniform distribution function. This ensured an equal probability of selecting the location of the pore in the 3D pore microstructure and an equal probability in the degree of overlap between the pores. Two controls were then applied. The first control was to ensure that the first pore is centred in the 3D pore microstructure. This guarantees that the pores are not concentrated in certain regions of the 3D pore microstructures, allowing the pore networks to spread out inside the respective rock domains. The second control was to ensure that all the pores were connected; hence porosity is equivalent to effective porosity in this study. The generation of the 3D pore microstructures was automated and run on Oklahoma State University's Pete Supercomputer, which provided 32 cores and 96 GB of RAM for each run. It took 5–35 min to generate each 3D pore microstructure.

The rock domain within which the 3D pore microstructures are generated is a cube (Fig. 1) with varied length scale across the three groups. This is due to the need to have a relatively fixed effective porosity, PSD, and number of pores in each group. To verify that the varying length scales do not impact the study, a representative elementary volume (REV) analysis was conducted (Bear, 1972). This analysis has been used in several studies to justify that macroscopic properties (e.g., porosity, organic matter content, and specific surface area) are not controlled by sample volume (Mostaghimi et al., 2012; Peng et al., 2012; Saraji and Piri, 2015; Wu et al., 2017). For this study, the REV analysis was conducted based on average pore size to guarantee that the pore size distribution and porosity is consistent for

Table 1
Statistical analysis of permeability.

Group	Mean pore size (μm)	Standard deviation of PSD (μm)	Mean Permeability (mD)	CV of Permeability	Skewness	Kurtosis
I	10	0	28.47	24%	0.57	3.59
II	10	5	6.39	44%	2.32	16.27
III	10	11	0.27	161%	6.24	62.97

pore-microstructures in each group. Here, the number of pores in the 3D pore microstructures is sufficient when the difference between the averages of the pores sizes is insignificant as the number of pores is increased further. Furthermore, the mean of the PSD used to generate the data set is known (10 μm); therefore, the mean pore size at REV must be closer to this number. The REV analysis was conducted for group III of 3D pore microstructures since this group constitutes the most severe scenario of heterogeneity; hence, it requires the largest number of pores to reach a representative value. Fig. 3 shows 700 pores to be representative for the range of pore sizes used in this study. By contrast, the average number of pores in this study is 973, resulting in a length scale of 133 μm for group I, 169 μm for group II, and 302 μm for group III of 3D pore microstructures.

2.2. Pore-scale simulations of flow

Simulation of incompressible flow through the generated 3D pore microstructures of stochastic pore connectivity was conducted with STAR-CCM+® which uses the finite volume methodology to solve the mass continuity equation:

$$\overrightarrow{\nabla}\cdot\rho\overrightarrow{V}+\frac{\partial\rho}{\partial t}=0 \tag{3}$$

and Navier-Stokes momentum equation:

$$\frac{\partial\overrightarrow{V}}{\partial t}+\left(\overrightarrow{V}\cdot\overrightarrow{\nabla}\right)\overrightarrow{V}=-\frac{1}{\rho}\overrightarrow{\nabla}P+\nu\overrightarrow{\nabla}^{2}\overrightarrow{V} \tag{4}$$

where ρ is density of the fluid, v is kinematic viscosity, P is pressure, t is time, and $\overrightarrow{V}$ is fluid velocity.

STAR-CCM+® has been shown in previous works to accurately replicate fundamental pore-scale flow (Yang et al., 2013, 2015) and solute transport processes (Yang et al., 2015; Oostrom et al., 2014). The first step in flow simulation was to conduct a mesh independence study to ensure that flow velocity profiles obtained from solving the governing equations (3) and (4) is independent of the mesh resolution. Twenty samples were randomly selected for this purpose. It involves steadily increasing the number of cells in a flow domain and computing the average velocity. A model is deemed mesh independent when the change in average velocity is insignificant for an increase in the minimum cell size (See Fig. S1 in the supplementary data). The final mesh was generated with a minimum cell size of 0.75 μm with other parameters at default. For this study, an unstructured polyhedral mesh type was used. This helped capture the complex nature of the 3D pore microstructures (Fig. 4).

The average number of cells per pore microstructure is 640,000 which ultimately results in an average computational time of 15 min per simulation. The governing equations (3) and (4) were solved for a steady state condition. For simplicity, the fluid used in the simulations was water with no chemical reaction between the fluid and the pore microstructures. The rock domain had closed boundaries except for two opposite sides through which flow was allowed. A stagnation inlet pressure condition was applied at the inlet with a fixed pressure of 1 Pa while an outlet pressure of 0 Pa is fixed at the outlet, maintaining a pressure drop of 1 Pa across the two open boundaries (Fig. 4).

A no-slip wall condition was applied to the remainder of the computational domain. The Reynolds number of the flow simulations were less than 0.0001 in all 3D pore-microstructures in this study. This makes the calculation of permeability with Darcy's law valid in all the generated 3D pore-microstructures (Chen et al., 2014). Each pore-scale numerical simulation reached steady state conditions before 150 iterations (See Fig. S2 in the supplementary data).

Simulations are stopped at the 200th iteration and solutions are deemed to converge when the mass flow at the inlet and the outlet are equal and within 0.1% of the respective mass flow in the prior iteration. A secondary condition was also added to ensure that the residuals (continuity, x momentum, y momentum, and z momentum) are all less than 10^{-6}. This process was automated and run on the same supercomputing cluster used in generating the 3D pore microstructures.

2.3. Permeability estimation

Permeability was calculated from Darcy's equation (Vilcáez et al., 2017; Chen et al., 2014; Darcy, 1856). Mathematically, Darcy's equation is expressed as:

$$K=\frac{V\times\mu\times L}{\Delta P} \tag{5}$$

where V is the Darcy flow velocity in the rock domain in m/s, K is the absolute permeability of the rock domain in m^2, ΔP is the pressure drop in the principal direction of the fluid in Pa, μ is the dynamic viscosity of the fluid in Pa-s, and L is the length along the direction of the pressure drop in meters. Calculated permeability was converted from m^2 to mD. Darcy flow velocity can be rewritten as:

$$V=\frac{Q}{A} \tag{6}$$

where Q is the volumetric flowrate through the inlet or outlet in m^3/s and A is the cross-sectional area perpendicular to the flow at the respective boundary in m^2. Volumetric flowrate can also be rewritten as:

$$Q=\frac{M}{\rho} \tag{7}$$

where M is the mass flowrate through the inlet or outlet in kg/s and ρ is the density of the fluid flowing through the medium in $\mathrm{kg/m}^3$. Combining (6) and (7):

$$V=\frac{M}{A^{*}\rho} \tag{8}$$

Combining (5) and (8):

$$K=\frac{M\times\mu\times L}{\Delta P^{*}A^{*}\rho} \tag{9}$$

Since properties of the fluid (density and viscosity of water) and pressure drop are constant, permeability is calculated from mass flow rate and length scale (L^{-1}) of the digital rock domain.

2.4. Hydraulic tortuosity estimation

Hydraulic tortuosity can be calculated in terms of the flow velocity (Vilcáez et al., 2017; Duda et al., 2011):

$$\tau=\frac{V}{V_i} \tag{10}$$

where V is the average magnitude of the intrinsic velocity over the entire

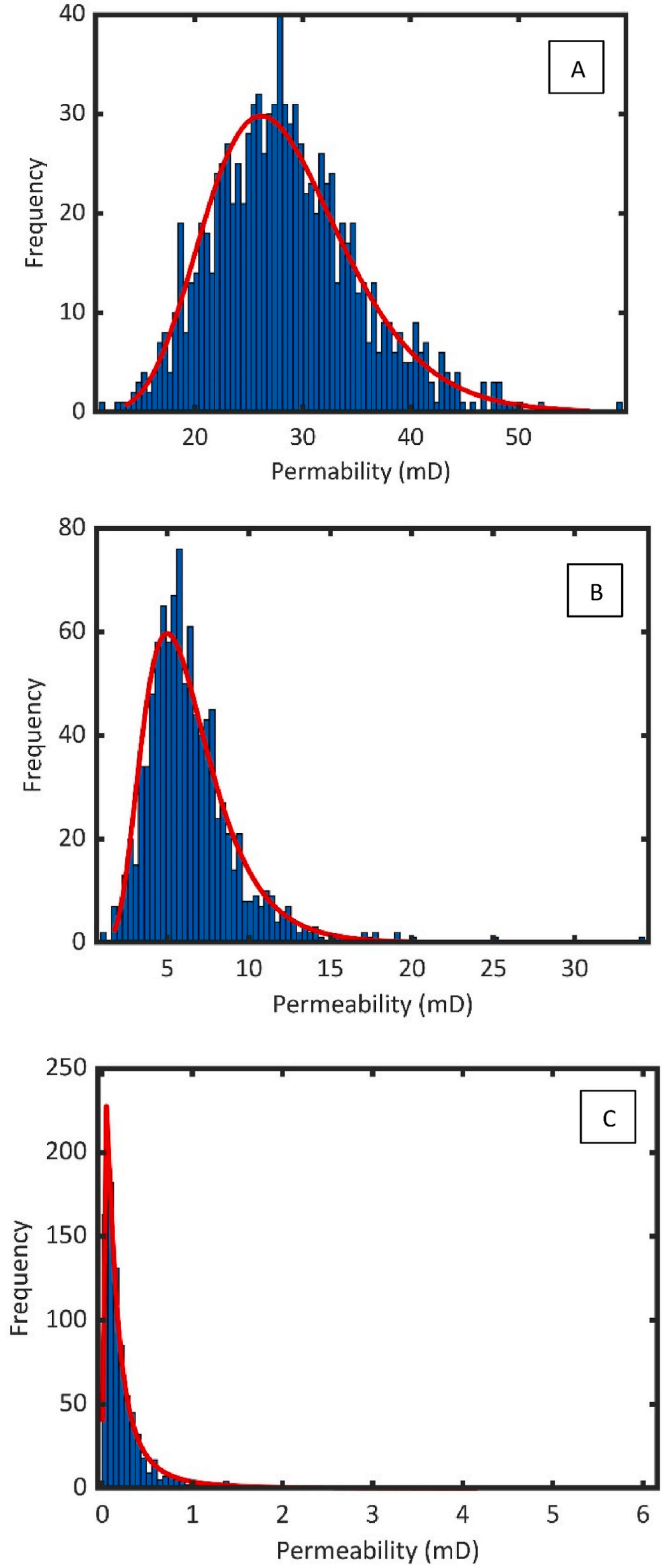

Fig. 7. A lognormal density function (red line) fitted on histograms of permeability distribution for (A) group I, (B) group II, and (C) group III.

system volume in m/s, and V_i is the volumetric average of the component parallel to the macroscopic flow direction in m/s.

By implication, the smallest possible hydraulic tortuosity is 1, which indicates a straight-line flow path. An increase in the hydraulic tortuosity value translates into more tortuous and longer flow path.

2.5. *Pore microstructural parameters*

To elucidate the effect of stochastic pore connectivity on permeability and hydraulic tortuosity of complex heterogeneous rocks, the following parameters were obtained from the generated 3D pore microstructures.

2.5.1. *Pore-throat sizes*

The pore-throat size is the length at the intersection between two pores (Fig. 5). Pore-throats sizes are constrained by the sizes of the pore they connect since a pore-throat cannot be larger than the size of the pores they are connecting. The size of the pore-throats for each group of 3D pore microstructures were calculated, resulting in a relatively uniform pore-throat size distribution (PTSD) for 3D pore microstructures constructed from uniform PSD (Fig. 6A) and a lognormal PTSD for 3D pore microstructures constructed from lognormal PSD (Fig. 6B and C).

2.5.2. *Surface area*

The surface area (S) of each 3D pore microstructure was calculated. Although surface area is not a direct subject of this study, it plays a key role in the velocity distribution in porous media. This is because of the no-slip condition at the pore-fluid boundary resulting in zero velocity at the pore walls. Therefore, it has an inverse relationship with the average flow velocity through porous media which is consequential for permeability and hydraulic tortuosity.

Two parameters were derived from the surface area, namely pore volume normalized surface area (pS) which is given by:

$$pS = \frac{S}{P} \tag{11}$$

and bulk volume normalized surface area (bS) which is given by:

$$bS = \frac{S}{B} \tag{12}$$

where S, P, and B are the surface area of pores (m^2), pore volume (m^3), and the bulk volume of the digital rock (m^3) respectively.

2.6. *Neural network implementation*

A feedforward neural network (NN) was applied to assess the predictability of permeability and hydraulic tortuosity using PTSD data and surface area parameters. Ten features were used for training the NN algorithm. This includes bulk volume normalized surface area (bS), pore volume normalized surface area (pS), standard deviation of the PTSD, 1st percentile of the PTSD, 10th percentile of the PTSD, 25th percentile of the PTSD, 50th percentile of the PTSD, 75th percentile of the PTSD, 90th percentile of the PTSD, and domain length scale. The domain length scale accounts for the different length scales of the three groups of 3D pore microstructures. The targets are permeability and hydraulic tortuosity. Correlation between all the features and targets were examined in each group to help evaluate the predictability of the targets from individual features and identify possible multicollinearity between features used in this study (See Table S1, S2 and S3 in the supplementary data). The features and targets from the three groups were combined for use in the NN algorithm to maximize its performance. In the preprocessing stage of the NN algorithm deployment, the data was randomly split into training, validation, and test data in a 7:1:2 ratio, respectively. The data was randomly sampled to remove bias and the percentage of training data is deemed sufficient given the total size of our data (Verdhan, 2020). The training data was used to train the NN algorithm while the validation data were used to check the predictability of the target properties with the NN algorithm after each epoch to guard against overfitting. The test data was finally used to check the predictability of permeability and hydraulic tortuosity from the trained NN algorithm. Prior to training, the features were standardized using the

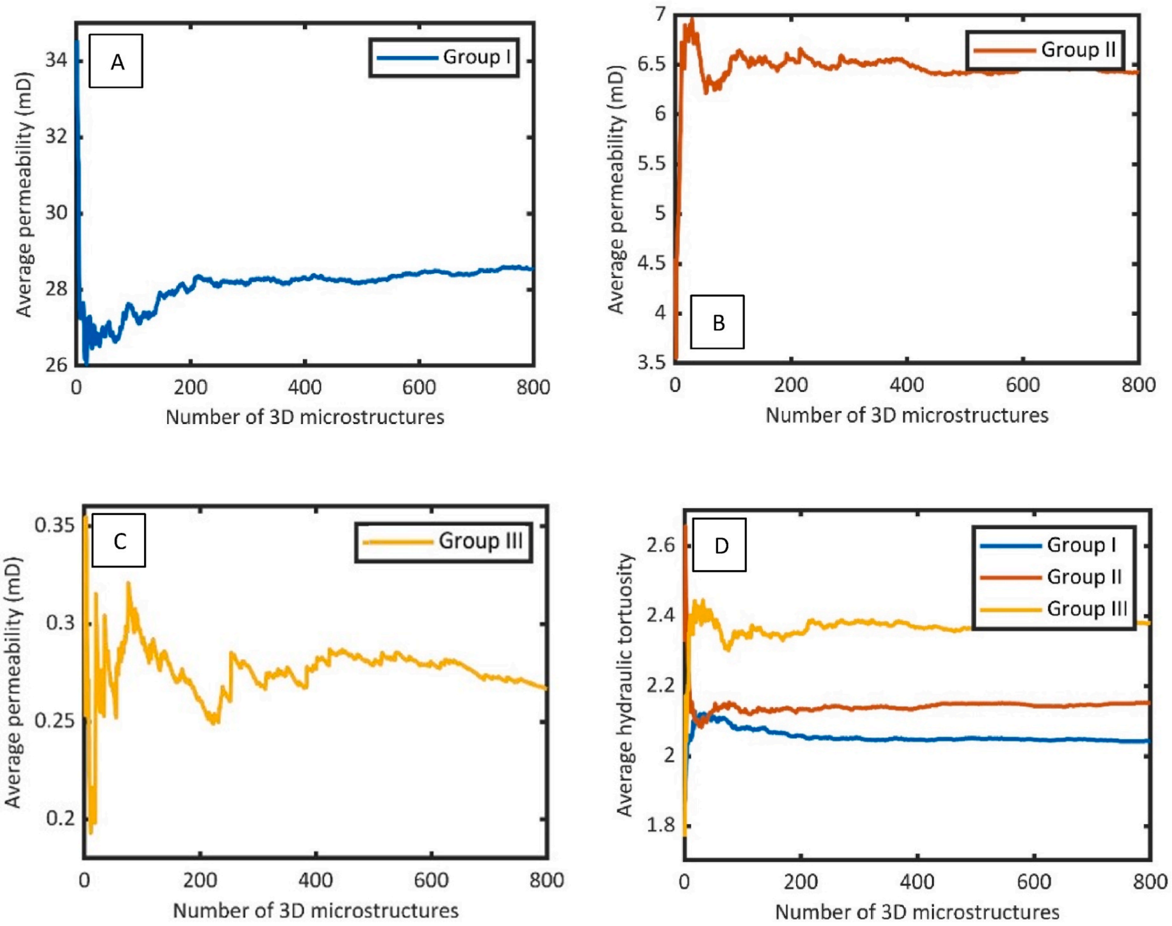

Fig. 8. A, B, and C shows the change in average permeability with the number of 3D pore microstructures while D shows the change in average hydraulic tortuosity with the number of 3D pore microstructures.

z-scoring technique (Mohamad and Usman, 2013). The NN architecture of the permeability model used in this study comprised of an input layer, two hidden layers with 64 neurons each, an output layer, and a 10% dropout before the output layer as a second measure to prevent overfitting. The two hidden layers in the permeability model were assigned sigmoid activation functions. For the hydraulic tortuosity model, the NN architecture is made up of an input layer, a single hidden layer with 64 neurons and tanh activation function, and an output layer. The loss function used in both models is the mean squared error which was minimized with the Adam optimizer (Kingma and Ba, 2014) at a learning rate of 0.001. The choices of activation function, number of neurons, and number of hidden layers were based on comparative performance when tuning the hyperparameters. A linear activation function was used as output since both target properties are continuous values. The epoch was set to 20,000 with a patience of 100. The best training weights was selected based on the mean squared error of the validation data.

3. Results and discussion

3.1. Heterogeneity and permeability

Table 1 summarizes mean permeability values estimated for groups I, II, and III of 3D pore microstructures of different degree of heterogeneity (pore size standard deviation).

As expected, an increase in the degree of heterogeneity (pore size standard deviation) reduces permeability because effective porosity and the number of pores in all generated 3D pore microstructures is approximately the same. If effective porosity and the number of pores is the same, an increase in heterogeneity results in an increase of the number of smaller pore-throats as shown in Fig. 6. Since pore-throat sizes are generally smaller when heterogeneity is increased and pore-throats are always smaller than pore bodies (Fig. 5), it is apparent that PTSD is a key control of permeability. An approximate twofold increase in heterogeneity (pore size standard deviation) from group I to group III results in decrease of the mean pore-throat size from 5.99 µm to 3.79 µm (Fig. 6) and a two orders of magnitude reduction in average permeability from 28.5 mD to 0.27 mD (Table 1).

The resulting lognormal permeability distribution (Fig. 7) has been reported for real rocks (Malin et al., 2020; Sahin et al., 2007) validating the stochastic pore-scale simulation approach used in this study. A key contribution of this study is that an increase in heterogeneity also results in an increase of the skewness and kurtosis of the permeability distribution curves (Fig. 7) which represents a systematic shift of permeability from normal distribution to lognormal distribution. This also results in an increase in the CV of permeability from 24% to 161% (Table 1). Fig. 8 shows that the average permeability for each group does not significantly change when the number of generated 3D pore microstructures is more than 300, indicating that representative nature of this analysis.

By implication, the use of Gaussian techniques to obtain permeability realizations using geostatistics (e.g., Kriging) is not recommended in modelling and simulations of fluid flow. The larger the standard deviation of pore size in the PSD of a rock, the more skewed and long tailed the distribution of permeability that can be associated to the rock.

Furthermore, variation in the permeability of group I with uniform

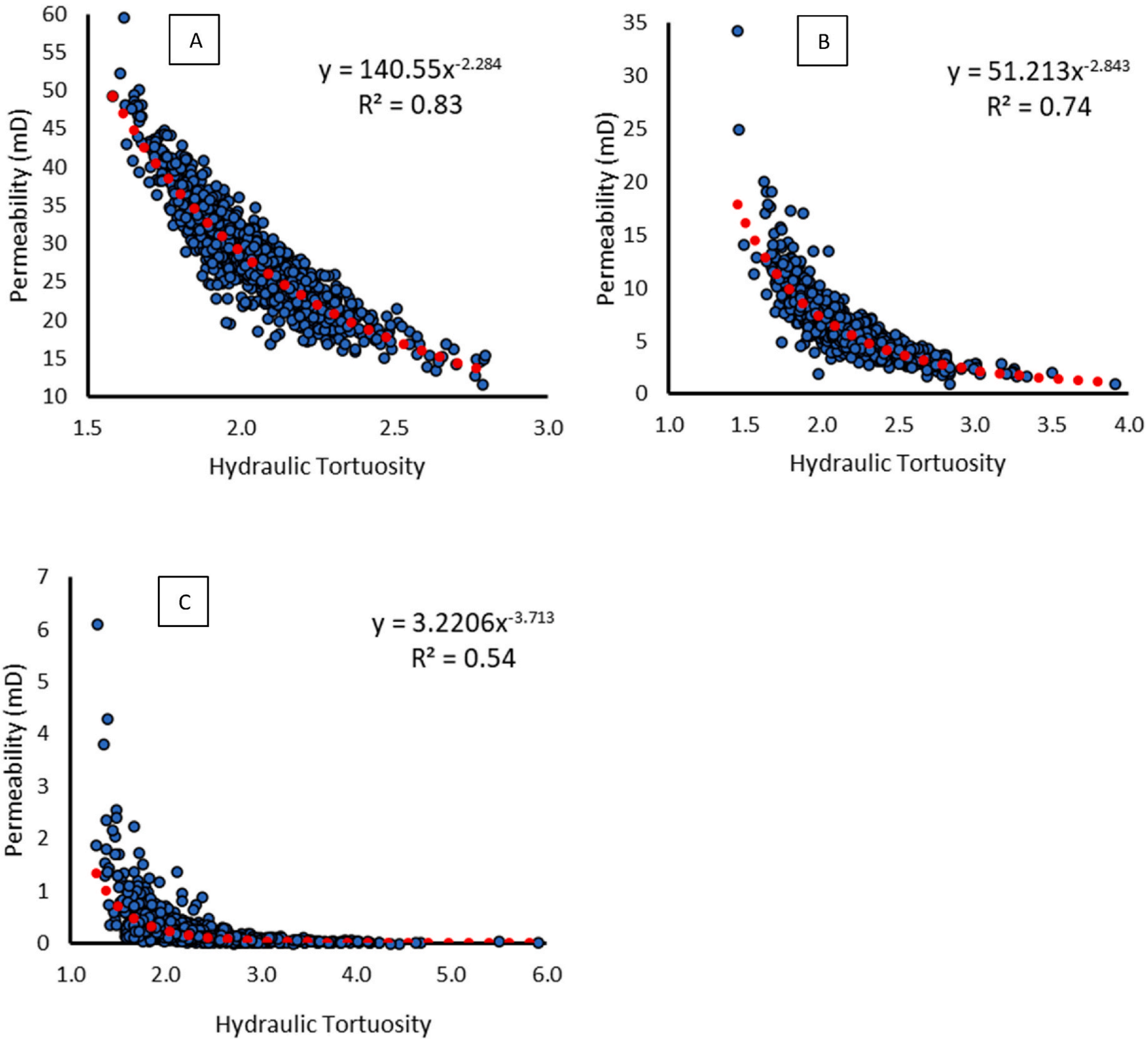

Fig. 9. Hydraulic tortuosity against permeability for A) group I, B) group II, and C) group III. The red dotted line is the best data fit which is power law.

Table 2
Statistical analysis of hydraulic tortuosity.

Group	**Mean pore size (μm)**	Standard deviation of PSD (μm)	**Mean Hydraulic Tortuosity**	**CV of Hydraulic Tortuosity**	**Skewness**	**Kurtosis**
I	10	0	2.05	10%	0.62	3.82
II	10	5	2.16	13%	1.05	5.93
III	10	11	2.38	25%	1.21	5.94

PSD is an indication that PSD is not enough to accurately predict the permeability of rocks. This is because even if pore size is the same, pore-throat size is varying due to the stochastic nature of pore connectivity (Fig. 6A). Hence, it is more reliable to obtain permeability prediction from PTSD compared to the use of porosity and/or PSD.

Heterogeneity also impacts the relationship between permeability and hydraulic tortuosity. Fig. 9 shows the predictability of permeability from hydraulic tortuosity to decrease with an increase in heterogeneity. The deteriorating relationship is evident from the decreasing R^2 value. Therefore, equations that leverage on the relationship between permeability and hydraulic tortuosity such as the Kozeny (1927) and Kozeny-Carman models (Carman, 1937) might give misleading estimates of flow properties in heterogeneous porous media.

3.2. Heterogeneity and hydraulic tortuosity

Table 2 summarizes mean hydraulic tortuosity values estimated for groups I, II, and III of 3D pore microstructures of different degree of heterogeneity (pore size standard deviation). An increase in heterogeneity increases the average hydraulic tortuosity in each group.

This is expected given the inverse relationship between heterogeneity and permeability (Table 1) and the inverse relationship between hydraulic tortuosity and permeability (Fig. 9). Fig. 8 shows that the average hydraulic tortuosity does not significantly change after 300 samples, indicating the representative nature of this study. Like the distribution of permeability, the distribution of hydraulic tortuosity is more skewed and long tailed (Table 2 and Fig. 10) as heterogeneity (standard deviation of PSD) increases from group I to group III (Fig. 1). However, it is still close to a normal distribution in the most severe case of heterogeneity (Fig. 10). Furthermore, there is only a small change in

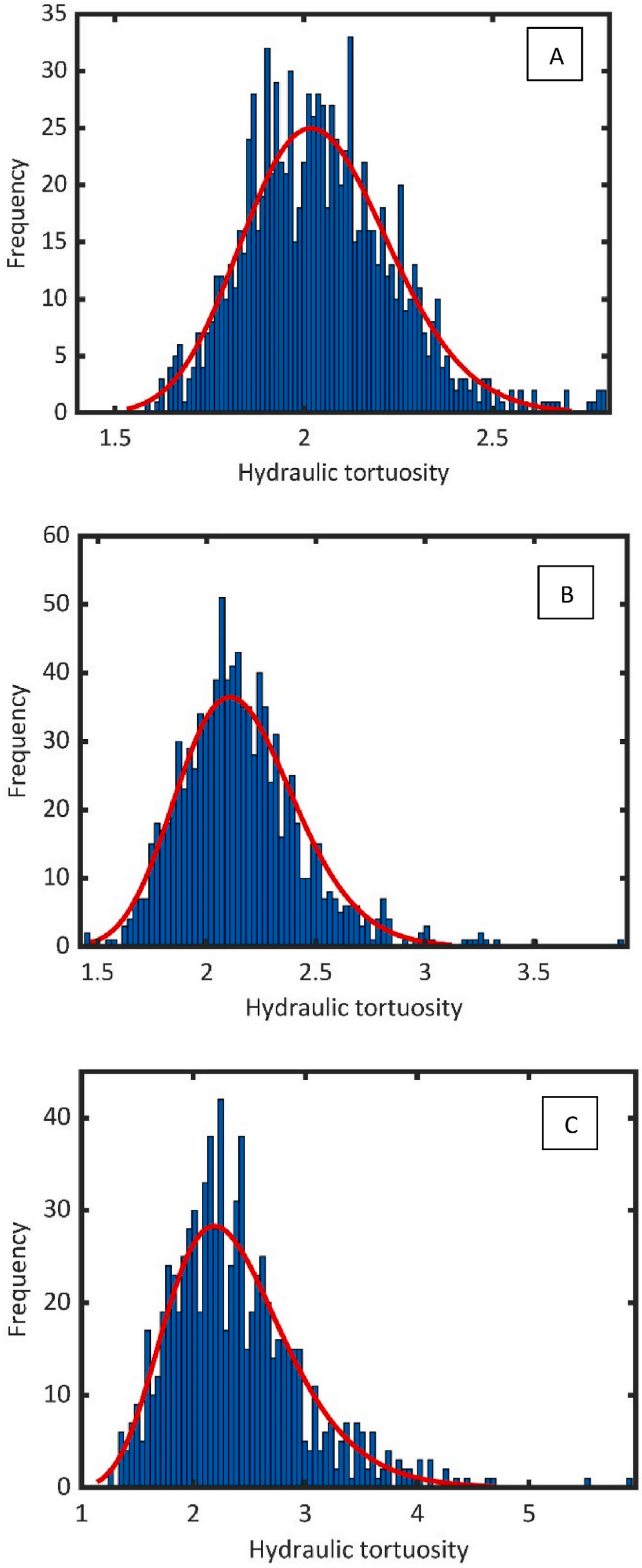

Fig. 10. A lognormal density function (red line) fitted on histograms of hydraulic tortuosity distribution for the stochastically generated 3D pore microstructures: (A) group I, (B) group II, and (C) group III.

mean hydraulic tortuosity across the three groups, implying that PTSD resulting from the random connectivity of pores does not have a significant effect on hydraulic tortuosity. However, it is noteworthy the results in Table 2 indicates that hydraulic tortuosity of rocks will generally vary even if the porosity and PSD is the same.

3.3. *Permeability and hydraulic tortuosity predictability with neural networks*

Fig. 11 compares direct pore-scale simulations and NN predictions of permeability and hydraulic tortuosity. The coefficient of determination (R2) of permeability and hydraulic tortuosity are 0.94 (Fig. 11.A) and 0.23 (Fig. 11.C) respectively.

The high coefficient of determination obtained with the use of the NN to predict permeability indicates NN algorithms trained using PTSD data and surface area parameters can significantly capture the stochastic nature of pore connectivity of real rocks. Furthermore, the addition of hydraulic tortuosity as a parameter in permeability prediction improves the R^2 metric from 0.94 to 0.98 (Fig. 11.A and 11.B).

Hydraulic tortuosity prediction with the corresponding NN model is poor. However, the coefficient of determination for hydraulic tortuosity prediction increases from 0.24 to 0.50 when permeability is added to the training parameters (Fig. 11.C and 11.D). It is worth noting that the mean absolute error of the test data is only 0.23 without permeability as a parameter and 0.17 when permeability is added as a parameter. These errors are very small compared to the ranges of possible hydraulic tortuosity, up to 4.5 (Fig. 10) for a single porosity value that was used in this study, underlying the merits of using NN with parameters selected in this study compared to model equations that estimate hydraulic tortuosity directly from porosity.

The use of NN model for prediction of permeability and hydraulic tortuosity as used in this study is practical since PTSD data, surface area parameters, and domain length can be obtained from MICP measurements and routine analysis. The inclusion of permeability-hydraulic tortuosity relationship in the respective NN models has been shown to be beneficial (Fig. 11); however, it might also have a negative effect on performance if model is not properly trained (Fig. 12). At smaller epochs, the inclusion of permeability-hydraulic tortuosity relationships in both NN models could worsen performance (Fig. 12). Hence, establishing an optimal number of epoch is very vital.

4. Conclusions

This study has employed a stochastic pore-scale simulation approach to statistically elucidate the effect of stochastic pore connectivity on permeability and hydraulic tortuosity of highly heterogeneous porous media such as carbonate rocks. Furthermore, we assessed the capacity of NN to capture the stochastic nature of pore connectivity. The novelty of this study lies in the generation of multiple pore microstructures where the only pore microstructural feature changing is pore connectivity, allowing the explicit study of the role of pore connectivity on flow without the interference of other factors. The key findings from this novel approach are as follow:

1. An increase in heterogeneity (pore size distribution) drives the distribution of permeability farther from normal distribution towards lognormal distribution. This can be crucial when introducing permeability heterogeneity into reservoir scale models of permeability. Like permeability, hydraulic tortuosity also deviates from normal distribution; however, the degree of divergence from normal distribution is insignificant.
2. Pore-throat size distribution and pore surface area obtainable from rock MICP data can be leveraged in machine learning algorithms such as feedforward neural networks to make predictions of permeability with a high degree of accuracy. On the other hand, hydraulic tortuosity is poorly predicted using the same approach

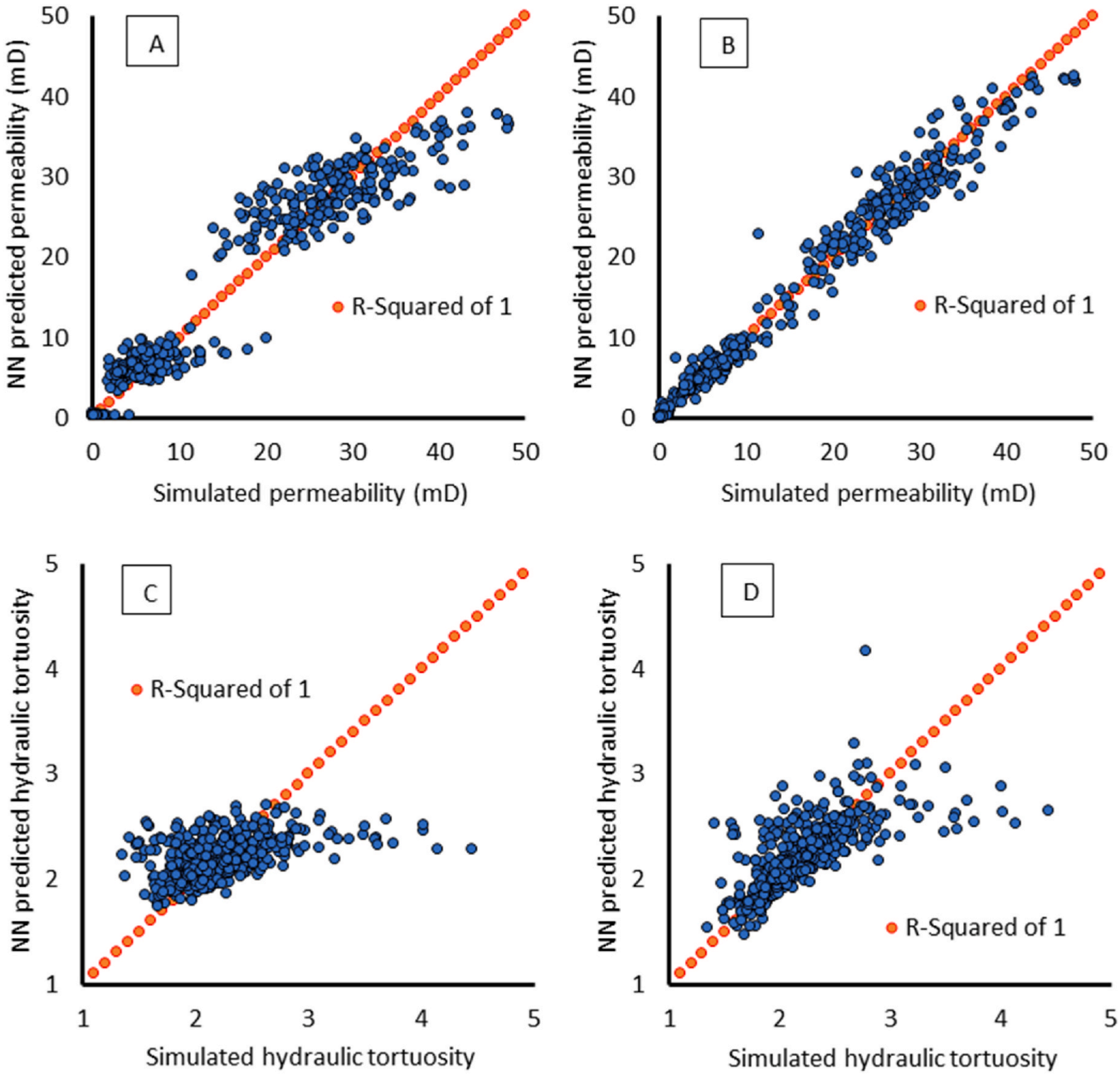

Fig. 11. Pore-scale simulations versus NN predictions of permeability and hydraulic tortuosity data. A) Permeability predictions made from surface are parameters (pS, bS), domain length scale, standard deviation of PTSD, and PTSD percentiles (1st, 10th, 25th, 50th, 75th, and 90th). B) Permeability predictions made with tortuosity added as a 11th parameter. C) Hydraulic tortuosity predictions made from pore microstructure parameters: pS, bS, domain length scale, standard deviation of PTSD, and PTSD percentiles (1st, 10th, 25th, 50th, 75th, and 90th). D) Hydraulic tortuosity predictions made with permeability added as a 11th parameter. The number of data point in each plot is 558.

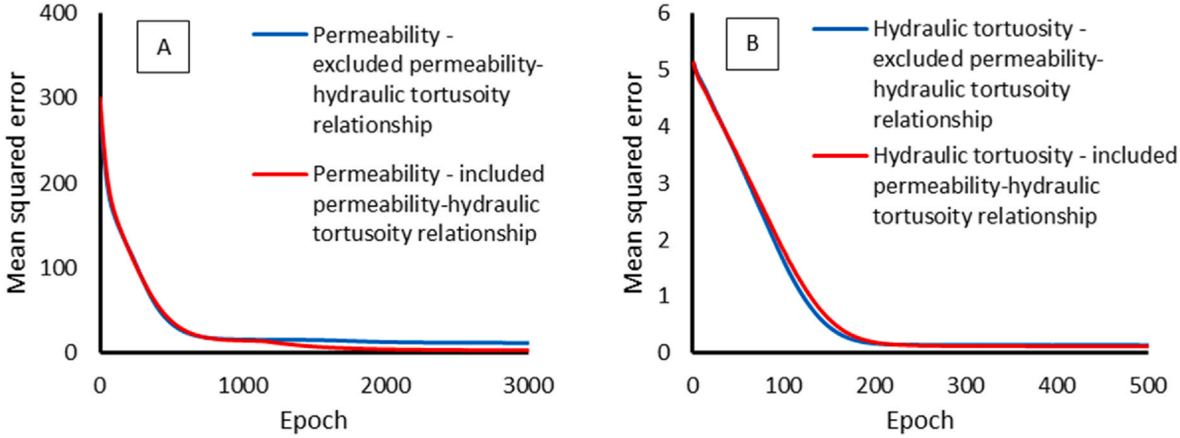

Fig. 12. Variation in MSE of validation data with epoch for A) the permeability NN model and B) the hydraulic tortuosity NN model.

which suggests that pore-throats or surface area are not the key controls of hydraulic tortuosity.

3. The use of NN could serve as an efficient alternative to direct pore-scale simulations of permeability which are computationally intensive.
4. In comparison to model equations that employ porosity and/or pore size distribution as the key predictive parameter for permeability and hydraulic tortuosity, the use of feedforward neural network provides a better prediction given the variability in permeability and hydraulic tortuosity obtained at a fixed porosity and pore size distribution particularly when heterogeneity is high.
5. The relationship between permeability and hydraulic tortuosity deteriorates with increase in heterogeneity. Therefore, deterministic equations that relate permeability and hydraulic tortuosity (for example, the Kozeny-Carman equation) might be less reliable at higher degrees of heterogeneity in rocks.

In general, the outcome of this statistical and neural network analysis helps improve our understanding about the effect of heterogeneity and pore connectivity on fluid flow and solutes transport. This insight has a broader significance in enhanced oil recovery, geological carbon storage, petroleum produced water disposal, resource exploration and production, as well as the management of subsurface environment. Furthermore, it introduces a way to leverage the use of MICP data to make relatively accurate predictions of permeability and hydraulic tortuosity. In a follow up study, the established pore-scale stochastic approach will be used to predict permeability of actual carbonate rocks at Darcy's scale.

Author statement

Olubukola Ishola: Investigation, Methodology, and Writing - Original Draft. Aaron Alexander: Software. Javier Vilcáez: Conceptualization, Supervision, Project administration, Funding acquisition, Writing - Review & Editing.

Funding source

This material is based upon work supported by the National Science Foundation under Grant HS-2041648.

Declaration of competing interest

The authors declare the following financial interests/personal relationships which may be considered as potential competing interests: Javier Vilcáez reports financial support was provided by National Science Foundation.

Acknowledgments

We appreciate the Association of Petroleum Geologist Foundation (AAPG), Oklahoma Geological Foundation (OGF), and the Oklahoma City Section of Society of Petroleum Engineers (SPE) for partial financial support of the Ph.D. research of the first author. This is Oklahoma State University Boone Pickens School of Geology contribution number 2022-129. Some of the computing for this project was performed at the High-Performance Computing Center at Oklahoma State University (OSU).

Appendix A. Supplementary data

Supplementary data to this article can be found online at https://doi.org/10.1016/j.jngse.2022.104719.

References

Al Khalifah, H., Glover, P.W.J., Lorinczi, P., 2020. Permeability prediction and diagenesis in tight carbonates using machine learning techniques. Mar. Petrol. Geol. 112.

Algive, L., et al., 2012. Impact of diagenetic alterations on the petrophysical and multiphase flow properties of carbonate rocks using a reactive pore network modeling approach. Oil Gas Sci. Technol. – Rev. IFP Energies nouvelles 67 (1), 147–160.

Anovitz, L.M., Cole, D.R., 2015. Characterization and analysis of porosity and pore structures. Rev. Mineral. Geochem. 80 (1), 61–164.

Apostolopoulou, M., et al., 2019. Estimating permeability in shales and other heterogeneous porous media: deterministic vs. stochastic investigations. Int. J. Coal Geol. 205, 140–154.

Baychev, T.G., et al., 2019. Reliability of algorithms interpreting topological and geometric properties of porous media for pore network modelling. Transport Porous Media 128 (1), 271–301.

Bear, J., 1972. Dynamics of Fluids in Porous Media. American Elsevier Publishing Company.

Bernabé, Y., Li, M., Maineult, A., 2010. Permeability and pore connectivity: a new model based on network simulations. J. Geophys. Res. 115 (B10).

Bijeljic, B., Mostaghimi, P., Blunt, M.J., 2013. Insights into non-Fickian solute transport in carbonates. Water Resour. Res. 49 (5), 2714–2728.

Blunt, M.J., et al., 2013. Pore-scale imaging and modelling. Adv. Water Resour. 51, 197–216.

Carman, P., 1937. Fluid flow through granular beds. Chem. Eng. Res. Des. (15), 150–166.

Chen, Y., et al., 2014. Role of pore structure on liquid flow behaviors in porous media characterized by fractal geometry. In: Chemical Engineering and Processing: Process Intensification.

Chen, Y., et al., 2015. Role of pore structure on liquid flow behaviors in porous media characterized by fractal geometry. Chem. Eng. Process: Process Intensif. 87, 75–80.

Cheng, Z., et al., 2019. The effect of pore structure on non-Darcy flow in porous media using the lattice Boltzmann method. J. Petrol. Sci. Eng. 172, 391–400.

Choquette, P.W., Pray, L.C., 1970. Geologic Nomenclature and Classification of Porosity in Sedimentary Carbonates.

Clennell, M.B., 1997. Tortuosity: a guide through the maze. Geol. Soc. London Special Publ. 122 (1), 299–344.

Darcy, H., 1856. *Les fontaines publiques de la Ville de Dijon* V. Dalmont.

Dastidar, R., Sondergeld, C.H., Rai, C.S., 2007. An improved empirical permeability estimator from mercury injection for tight clastic rocks. Petrophysics 48 (3), 186–190.

Ding, B., et al., 2015. Effects of pore size distribution and coordination number on the prediction of filtration coefficients for straining from percolation theory. Chem. Eng. Sci. 127, 40–51.

Duda, A., Koza, Z., Matyka, M., 2011. Hydraulic tortuosity in arbitrary porous media flow. Phys. Rev. E - Stat. Nonlinear Soft Matter Phys. 84 (3 Pt 2), 036319.

Dutton, S.P., Loucks, R.G., 2010. Diagenetic controls on evolution of porosity and permeability in lower Tertiary Wilcox sandstones from shallow to ultradeep (200–6700m) burial, Gulf of Mexico Basin. *U.S.A.* Mar. Petrol. Geol. 27 (1), 69–81.

Ebrahimi, P., Vilcáez, J., 2018a. Petroleum produced water disposal: mobility and transport of barium in sandstone and dolomite rocks. Sci. Total Environ. 634, 1054–1063.

Ebrahimi, P., Vilcáez, J., 2018b. Effect of brine salinity and guar gum on the transport of barium through dolomite rocks: implications for unconventional oil and gas wastewater disposal. J. Environ. Manag. 214, 370–378.

Ebrahimi, P., Vilcáez, J., 2019. Transport of barium in fractured dolomite and sandstone saline aquifers. Sci. Total Environ. 647, 323–333.

England, W.A., Magoon, L.B., Dow, W.G., 1994. Secondary migration and accumulation of hydrocarbons. In: The Petroleum System—From Source to Trap. American Association of Petroleum Geologists, 0.

Erofeev, A., et al., 2019. Prediction of porosity and permeability alteration based on machine learning algorithms. Transport Porous Media 128 (2), 677–700.

Feng, R., Grana, D., Balling, N., 2021a. Variational inference in Bayesian neural network for well-log prediction. Geophysics 86 (3), M91–M99.

Feng, R., et al., 2021b. Bayesian convolutional neural networks for seismic facies classification. IEEE Trans. Geosci. Rem. Sens. 59 (10), 8933–8940.

Friedman, M., 1976. Porosity, permeability, and rock mechanics-a review. In: The 17th US Symposium on Rock Mechanics.

Graczyk, K.M., Matyka, M., 2020. Predicting porosity, permeability, and tortuosity of porous media from images by deep learning. Sci. Rep. 10 (1), 21488.

He, L., et al., 2014. Complex relationship between porosity and permeability of carbonate reservoirs and its controlling factors: a case study of platform facies in Pre-Caspian Basin. Petrol. Explor. Dev. 41 (2), 225–234.

Huang, J., et al., 2019. Compositional simulation of fractured shale reservoir with distribution of nanopores using coupled multi-porosity and EDFM method. J. Petrol. Sci. Eng. 179, 1078–1089.

Huang, X., Zhou, W., Deng, D., 2020. Validation of pore network modeling for determination of two-phase transport in fibrous porous media. Sci. Rep. 10 (1), 20852.

Jiang, C., Zhang, D., Chen, S., 2021. Lithology identification from well-log curves via neural networks with additional geologic constraint. Geophysics 86 (5), IM85–IM100.

Kamath, J., 1992. Evaluation of accuracy of estimating air permeability from mercury injection data. SPE Form. Eval. 7 (4), 304–310.

Kenyon, W.E., 1992. Nuclear magnetic resonance as a petrophysical measurement. Nucl. Geophys. 6 (2), 153–171.

Kimura, M., 2018. Prediction of tortuosity, permeability, and pore radius of water-saturated unconsolidated glass beads and sands. J. Acoust. Soc. Am. 143 (5), 3154–3168.

Kingma, D.P., Ba, J., 2014. Adam: A Method for Stochastic Optimization.

Kolodzie Jr., S., 1980. Analysis of pore throat size and use of the waxman-smits equation to determine ooip in spindle field, Colorado. In: SPE Annual Technical Conference and Exhibition. Society of Petroleum Engineers, Dallas, Texas, p. 10.

Kozeny, J., 1927. Ueber kapillare Leitung des Wassers im Boden. Sitzungsber Akad. Wiss 136, 271–306.

Lala, A.M.S., 2020. A novel model for reservoir rock tortuosity estimation. J. Petrol. Sci. Eng. 192, 107321.

Li, C.-X., Liu, M., Guo, B.-C., 2020. Classification of tight sandstone reservoirs based on NMR logging. Appl. Geophys. 16 (4), 549–558.

Malin, P.E., et al., 2020. Observational and critical state physics descriptions of long-range flow structures. Geosciences 10 (2).

Mendes, R., et al., 2002. Particle swarms for feedforward neural network training. In: Proceedings of the 2002 International Joint Conference on Neural Networks. IJCNN'02 (Cat. No. 02CH37290). IEEE.

Mohamad, I.B., Usman, D., 2013. Standardization and its effects on K-means clustering algorithm. Res. J. Appl. Sci. Eng. Technol. 6 (17), 3299–3303.

Mostaghimi, P., Blunt, M.J., Bijeljic, B., 2012. Computations of absolute permeability on micro-CT images. Math. Geosci. 45 (1), 103–125.

Munawar, M.J., et al., 2021. Upscaling reservoir rock porosity by fractal dimension using three-dimensional micro-computed tomography and two-dimensional scanning electron microscope images. J. Energy Resour. Technol. 143 (1).

Naraghi, M.E., Javadpour, F., 2015. A stochastic permeability model for the shale-gas systems. Int. J. Coal Geol. 140, 111–124.

Niu, Q., Zhang, C., 2018. Joint inversion of NMR and SIP data to estimate pore size distribution of geomaterials. Geophys. J. Int. 212 (3), 1791–1805.

Oostrom, M., et al., 2014. Pore-scale and continuum simulations of solute transport micromodel benchmark experiments. Comput. Geosci. 20 (4), 857–879.

Peng, S., et al., 2012. Using X-ray computed tomography in pore structure characterization for a Berea sandstone: resolution effect. J. Hydrol. 472–473, 254–261.

Pittman, E.D., 1992. Relationship of porosity and permeability to various parameters derived from mercury injection-capillary pressure curves for sandstone. AAPG (Am. Assoc. Pet. Geol.) Bull. 76 (2), 191–198.

Purcell, W., 1949. Capillary pressures - their measurement using mercury and the calculation of permeability therefrom. J. Petrol. Technol. 1 (2), 39–48.

Sahin, A., et al., 2007. Permeability anisotropy distributions in an upper jurassic carbonate reservoir eastern Saudi arabia. J. Petrol. Geol. 30 (2), 147–158.

Saraji, S., Piri, M., 2015. The representative sample size in shale oil rocks and nano-scale characterization of transport properties. Int. J. Coal Geol. 146, 42–54.

Shabani, B., Vilcáez, J., 2017. Prediction of CO2-CH4-H2S-N2 gas mixtures solubility in brine using a non-iterative fugacity-activity model relevant to CO2-MEOR. J. Petrol. Sci. Eng. 150, 162–179.

Shabani, B., Vilcáez, J., 2018. A fast and robust TOUGH2 module to simulate geological CO2 storage in saline aquifers. Comput. Geosci. 111, 58–66.

Shabani, B., Vilcáez, J., 2019. TOUGHREACT-CO2Bio – a new module to simulate geological carbon storage under biotic conditions (Part 1): the multiphase flow of CO2-CH4-H2-H2S gas mixtures. J. Nat. Gas Sci. Eng. 63, 85–94.

Shabani, B., Pashin, J., Vilcáez, J., 2020. TOUGHREACT-CO2Bio – a new module to simulate geological carbon storage under biotic conditions (Part 2): the bio-geochemical reactive transport of CO2-CH4-H2-H2S gas mixtures. J. Nat. Gas Sci. Eng. 76, 103190.

Soete, J., et al., 2017. Lattice Boltzmann Simulations of Fluid Flow in Continental Carbonate Reservoir Rocks and in Upscaled Rock Models Generated with Multiple-Point Geostatistics, vol. 2017. Geofluids, 7240524.

Song, S., et al., 2020. Geologist-level wireline log shape identification with recurrent neural networks. Comput. Geosci. 134.

Swanson, B.F., 1981. A simple correlation between permeability and mercury capillary pressures. J. Petrol. Technol. 33 (12), 2498–2504.

Tembely, M., AlSumaiti, A.M., Alameri, W.S., 2021. Machine and deep learning for estimating the permeability of complex carbonate rock from X-ray micro-computed tomography. Energy Rep. 7, 1460–1472.

Timur, A., 1968. An investigation of permeability, porosity, & residual water saturation relationships for sandstone reservoirs. Log. Anal. 9 (4), 10.

van der Land, C., et al., 2013. Modelling the permeability evolution of carbonate rocks. Mar. Petrol. Geol. 48, 1–7.

Verdhan, V., 2020. Supervised Learning with Python.

Vilcáez, J., 2015. Numerical modeling and simulation of microbial methanogenesis in geological CO2 storage sites. J. Petrol. Sci. Eng. 135, 583–595.

Vilcáez, J., 2020. Reactive transport modeling of produced water disposal into dolomite saline aquifers: controls of barium transport. J. Contam. Hydrol. 233, 103600.

Vilcáez, J., Morad, S., Shikazono, N., 2017. Pore-scale simulation of transport properties of carbonate rocks using FIB-SEM 3D microstructure: implications for field scale solute transport simulations. J. Nat. Gas Sci. Eng. 42, 13–22.

Walls, J.D., Amaefule, J.O., 1985. *Capillary Pressure And Permeability Relationships In Tight Gas Sands* SPE/DOE Low Permeability Gas Reservoirs Symposium.

Westphal, H., et al., 2005a. NMR measurements in carbonate rocks: problems and an approach to a solution. pure and applied geophysics. PAGEOPH 162 (3), 549–570.

Westphal, H., et al., 2005b. NMR measurements in carbonate rocks: problems and an approach to a solution. Pure Appl. Geophys. 162 (3), 549–570.

Whitten, E.H.T., 1977. Stochastic models in geology. J. Geol. 85 (3), 321–330.

Wu, T., et al., 2017. Multiscale pore structure and its effect on gas transport in organic-rich shale. Water Resour. Res. 53 (7), 5438–5450.

Xiong, Q., Baychev, T.G., Jivkov, A.P., 2016. Review of pore network modelling of porous media: experimental characterisations, network constructions and applications to reactive transport. J. Contam. Hydrol. 192, 101–117.

Yang, X., et al., 2013. Direct numerical simulation of pore-scale flow in a bead pack: comparison with magnetic resonance imaging observations. Adv. Water Resour. 54, 228–241.

Yang, X., et al., 2015. Intercomparison of 3D pore-scale flow and solute transport simulation methods. Adv. Water Resour. 95, 176–189.

Yang, L., et al., 2018. Analyzing the effects of inhomogeneity on the permeability of porous media containing methane hydrates through pore network models combined with CT observation. Energy 163, 27–37.

Zhang, L., 2013. Aspects of rock permeability. Front. Struct. Civ. Eng. 7 (2), 102–116.

Zhang, Z., Cai, Z., 2021. Permeability prediction of carbonate rocks based on digital image analysis and rock typing using random forest algorithm. Energy Fuels 35 (14), 11271–11284.

Zheng, H., et al., 2022. Multi-scale pore structure, pore network and pore connectivity of tight shale oil reservoir from Triassic Yanchang Formation, Ordos Basin. J. Petrol. Sci. Eng. 212.